

Asymmetry and Hopf bifurcation in spherical Couette flow

Chowdhury K. Mamun

Department of Chemical Engineering, University of Texas at Austin, Austin, Texas 78712

Laurette S. Tuckerman

Department of Mathematics and Center for Nonlinear Dynamics, University of Texas at Austin, Austin, Texas 78712

(Received 19 April 1994; accepted 8 September 1994)

Spherical Couette flow is studied with a view to elucidating the transitions between various axisymmetric steady-state flow configurations. A stable, equatorially *asymmetric* state discovered by Bühler [Acta Mech. **81**, 3 (1990)] consists of two Taylor vortices, one slightly larger than the other and straddling the equator. By adapting a pseudospectral time-stepping formulation to enable stable and unstable steady states to be computed (by Newton's method) and linear stability analysis to be conducted (by Arnoldi's method), the bifurcation-theoretic genesis of the asymmetric state is analyzed. It is found that the asymmetric branch originates from a pitchfork bifurcation; its stabilization, however, occurs via a subsequent subcritical Hopf bifurcation. © 1995 American Institute of Physics.

I. INTRODUCTION

Spherical Couette flow—the flow between differentially rotating concentric spheres—is known to undergo transitions leading to axisymmetric vortices analogous to those in the classic cylindrical Taylor–Couette flow. In spherical Couette flow, Taylor vortices form only in the immediate neighborhood of the equator, and the maximum number of vortices is set by the nondimensional gap width defined by $\sigma \equiv (r_2 - r_1)/r_1$, where r_1 and r_2 are the radii of the inner and outer spheres. For the medium-gap cases discussed in this article, states are observed with zero, one, or two vortices in each hemisphere. [Nonaxisymmetric flows are also observed (e.g., Refs. 1–3) but these will not be discussed here.]

Experimental and numerical work has highlighted the role played by equatorial symmetry-breaking in the transitions in spherical Couette flows. Notably, an outstanding puzzle raised by the experimental work of Wimmer¹ concerning the one-vortex flow was resolved by symmetry-breaking: Numerical calculations^{4–7} showed that for $\sigma=0.18$ the transition from the zero-vortex to the one-vortex flow (both equatorially symmetric states) occurred via an asymmetric transition caused by a subcritical pitchfork bifurcation.

More recently, Bühler¹ numerically and experimentally surveyed a large Reynolds number range ($0 \leq \text{Re} \leq 2500$) for the gap width $\sigma=0.154$ and discovered a *stable, equatorially asymmetric state*. Although it resembles a symmetric state with one vortex on either side of the equator, in the asymmetric version one vortex is larger than the other and straddles the equator.

Generically, in a system with reflection symmetry, one would expect an asymmetric state to arise from a pitchfork bifurcation undergone by a closely related symmetric state. Indeed, Bühler found that the symmetric one-vortex branch ceased to exist or be stable at the lower end of his approximate existence range for the asymmetric state. The obvious scenario would be a pitchfork bifurcation, via which the

symmetric one-vortex state would be destabilized in favor of the asymmetric one-vortex states. Transitions would occur from each state to the other, possibly with a slight hysteresis.

However, this is not the case. Time-dependent computations instead show jumps to a *two-vortex state*, both from the symmetric one-vortex state (by increasing Re) and from the asymmetric state (by decreasing Re). A different, less straightforward, account of the bifurcation-theoretic origin of Bühler's asymmetric states is therefore necessary, and it is this task which we now undertake.

II. NUMERICAL METHODS

To fully understand the bifurcation-theoretic structure of solutions to a set of nonlinear evolution equations, three types of information are desirable. The first, and most often used in fluid dynamics, is the time evolution of the system from various initial conditions. These constitute the physically realizable phenomena to be explained. The second type of information is the set of steady-state solutions. For equations describing medium and high Reynolds number hydrodynamic systems, the number of steady states can be vast; however it is useful to obtain as much of the picture as possible, especially concerning unstable steady states. The third type of information is the eigenspectrum of the steady states. Leading eigenvalues are associated with transitions and loss of stability.

These three types of information are usually obtained by separate analyses, involving separate codes and researchers. Here we propose a unified computational approach to the three types of calculation, all based on a single time-dependent code and using the same set of low-level routines. We can readily transfer flow fields between each of the three computational tools: Time-dependent simulations can be used to generate initial states for branch continuation. Unstable steady states, possibly perturbed by the addition of eigenvectors, can serve as initial conditions for time evolution. Suspected bifurcations can be confirmed by linear stability analysis.

The remainder of Sec. II describes our numerical methods, and can be skipped without loss of continuity by readers wishing to pass directly to the results.

A. Governing equations and spatial discretization

The three calculations use the basic routines and spatial discretization described in Marcus and Tuckerman.⁸ We use a streamfunction-vorticity formulation to represent the axisymmetric velocity field \mathbf{U} in terms of two scalar fields. The first field, ω , is obtained from the azimuthal velocity U_ϕ by subtracting the solution to the Stokes problem:

$$\omega \equiv U_\phi - \frac{\Omega r_1^3 (r_2^3 - r^3)}{r^2 (r_2^3 - r_1^3)} \sin \theta.$$

Here Ω is the angular velocity of the inner sphere at r_1 (the angular velocity of the outer sphere at r_2 is zero). Hence ω satisfies homogeneous boundary conditions:

$$\omega = 0 \quad \text{at} \quad r = r_1, r_2.$$

The second field is the meridional streamfunction ψ such that

$$U_r \mathbf{e}_r + U_\theta \mathbf{e}_\theta = \nabla \times \psi \mathbf{e}_\phi = \nabla(\psi r \sin \theta) \times \frac{\mathbf{e}_\phi}{r \sin \theta}. \quad (1)$$

In order that $U_r, U_\theta = 0$ at $r = r_1, r_2$, the streamfunction obeys both Dirichlet and Neumann homogeneous boundary conditions:

$$\psi = \partial_r \psi = 0 \quad \text{at} \quad r = r_1, r_2.$$

The equations by which ω and ψ evolve are obtained by taking the azimuthal component of the Navier–Stokes equations and of their curl:

$$\partial_t \omega = N^\phi(\mathbf{U}) + \frac{1}{\text{Re}} \tilde{\nabla}^2 \omega, \quad (2)$$

$$\partial_t \tilde{\nabla}^2 \psi = N^\psi(\mathbf{U}) + \frac{1}{\text{Re}} \tilde{\nabla}^4 \psi. \quad (3)$$

In (2)–(3), length and time have been nondimensionalized by r_1 and Ω^{-1} , respectively, and the Reynolds number defined as $\text{Re} = r_1^2 \Omega / \nu$, with ν the kinematic viscosity. The elliptic operator $\tilde{\nabla}^2$ is defined by

$$\tilde{\nabla}^2 f \equiv \mathbf{e}_\phi \cdot \nabla^2 (f \mathbf{e}_\phi) = \left(\nabla^2 - \frac{1}{r^2 \sin^2 \theta} \right) f$$

and the nonlinear terms are

$$N^\phi(\mathbf{U}) \equiv \mathbf{e}_\phi \cdot \mathbf{U} \times (\nabla \times \mathbf{U}), \quad (4)$$

$$N^\psi(\mathbf{U}) \equiv -\mathbf{e}_\phi \cdot \nabla \times (\mathbf{U} \times (\nabla \times \mathbf{U})). \quad (5)$$

For numerical computations, the functions ω and ψ are represented by Chebyshev-sine series

$$f(r, \theta) = \sum_{l=0}^{M_r} \sum_{m=1}^{M_\theta} f_{lm} T_l \left(\frac{2r - r_1 - r_2}{r_2 - r_1} \right) \sin(m\theta). \quad (6)$$

Spatial derivatives are calculated by differentiating (6). The multiplications in the nonlinear terms (4)–(5) are carried out in a gridspace representation obtained by fast Chebyshev and

sine transforms.⁹ Typically, we use $M_r = 16$ radial modes or gridpoints and $M_\theta = 128$ angular modes or gridpoints, although for higher Reynolds numbers, we double the resolution in each direction. With two fields, a total of $M \equiv 2 \times M_r \times M_\theta$ values are used to represent a velocity field.

B. Time stepping

Time stepping is carried out by a Crank–Nicolson Adams–Bashforth algorithm:

$$\omega(t + \Delta t) = \left(I - \frac{\Delta t}{2 \text{Re}} \tilde{\nabla}^2 \right)_D^{-1} \left[\left(I + \frac{\Delta t}{2 \text{Re}} \tilde{\nabla}^2 \right) \omega(t) + \frac{\Delta t}{2} (3N^\phi(\mathbf{U}(t)) - N^\phi(\mathbf{U}(t - \Delta t))) \right], \quad (7)$$

$$\psi(t + \Delta t) = \left(\left(I - \frac{\Delta t}{2 \text{Re}} \tilde{\nabla}^2 \right) \tilde{\nabla}^2 \right)_{ND}^{-1} \left[\left(1 + \frac{\Delta t}{2 \text{Re}} \tilde{\nabla}^2 \right) \times \tilde{\nabla}^2 \psi(t) + \frac{\Delta t}{2} (3N^\psi(\mathbf{U}(t)) - N^\psi(\mathbf{U}(t - \Delta t))) \right]. \quad (8)$$

The subscript D means that homogeneous Dirichlet boundary conditions are applied in inverting the second-order operator in (7). The subscript ND means that both homogeneous Neumann and Dirichlet boundary conditions are imposed on ψ in inverting the fourth-order operator in (8), via an influence-matrix or Green's function technique.⁸

C. Steady-state solving

Steady-state solving by Newton iteration is rendered efficient by an adaptation of the time-stepping code, as described in Ref. 10. To explain the difficulty of a straightforward application of Newton's method and our resolution of the problem, we first write the Navier–Stokes equations in an abbreviated form as

$$\frac{d\mathbf{U}}{dt} = \mathbf{N}(\mathbf{U}) + \mathbf{L}\mathbf{U} \equiv \mathbf{A}\mathbf{U} \quad (9)$$

where \mathbf{N} and \mathbf{L} are the (spatially discretized) nonlinear and linear operators, respectively, and \mathbf{U} is the velocity field. The goal of the steady-state code is to solve

$$0 = \mathbf{N}(\mathbf{U}) + \mathbf{L}\mathbf{U}. \quad (10)$$

Newton's method for solving (10) is

$$(\mathbf{N}_U + \mathbf{L})\mathbf{u} = (\mathbf{N} + \mathbf{L})(\mathbf{U}), \quad \mathbf{U} \leftarrow \mathbf{U} - \mathbf{u} \quad (11)$$

The notation $\mathbf{N}_U + \mathbf{L}$ represents the linearization of $\mathbf{N} + \mathbf{L}$ about the current guess \mathbf{U} , i.e., the Jacobian. The action of this operator is calculated by replacing the nonlinear terms $\mathbf{N}^\phi(\mathbf{U})$ and $\mathbf{N}^\psi(\mathbf{U})$ in (4) and (5) by

$$\mathbf{N}_U^\phi \mathbf{u} = \mathbf{e}_\phi \cdot (\mathbf{U} \times \nabla \times \mathbf{u} + \mathbf{u} \times \nabla \times \mathbf{U}), \quad (12)$$

$$\mathbf{N}_U^\psi \mathbf{u} = -\mathbf{e}_\phi \cdot \nabla \times (\mathbf{U} \times \nabla \times \mathbf{u} + \mathbf{u} \times \nabla \times \mathbf{U}). \quad (13)$$

It is the storage and inversion of the Jacobian matrix which constitute the stumbling block in a steady-state calcu-

lation. Our flows are typically represented by $M=4096$ unknowns, so the Jacobian matrix is 4096×4096 . (For the finer resolution used at higher Re , $M=16384$.) The Jacobian matrix is not banded, which makes the cost of direct inversion proportional to an unmanageable M^3 . Iterative conjugate gradient methods for solving linear systems incur, in general, the same cost: a solution to the linear system is successively approximated by combining M multiplications of a vector by the matrix, each of which costs M^2 .

However, two factors can greatly reduce the cost of conjugate gradient solution: (1) The cost of multiplication by a matrix may be much less than $O(M^2)$, when the matrix is sparse or has a special structure. This is the case in our pseudospectral algorithm, where the multiplications in N_U are carried out in the gridspace representation and where the special structure of L in the Chebyshev-sine basis can be exploited.⁸⁻¹¹ Here, the cost of a matrix-vector multiplication is approximately proportional to M . (2) A matrix may be *well conditioned*, meaning that its condition number—roughly the ratio of largest to smallest eigenvalue—is close to one. Then, many fewer than M matrix-vector multiplications may be necessary to arrive at a converged solution to the linear system. Unfortunately, the Jacobian matrix arising from a discretization of the Navier–Stokes equations is almost invariably poorly conditioned. In such a case, one seeks a *preconditioner*, that is, a more easily accessible approximate inverse to the poorly conditioned matrix.

To understand our method of preconditioning, we first consider the reason for the poor conditioning of the Jacobian matrix. Its large range of eigenvalues originates primarily in the linear operator L , at least for the moderate Reynolds numbers associated with transition between different non-turbulent flows. The range of eigenvalues already poses a problem in solving the governing differential equations, where it implies a large range of time scales and is called *stiffness*. It is for this reason that the linear operators are treated *implicitly*, as, for example, in (7)–(8).

Our preconditioner will be based on a backwards-Euler forwards-Euler time-stepping scheme for integrating (9):

$$U(t + \Delta t) = (I - \Delta t L)^{-1} (I + \Delta t N) U(t) \equiv B U(t). \quad (14)$$

Taking the difference between successive time steps:

$$\begin{aligned} (B - I)U(t) &= U(t + \Delta t) - U(t) \\ &= (I - \Delta t L)^{-1} (I + \Delta t N) U(t) - U(t) \\ &= (I - \Delta t L)^{-1} (I + \Delta t N - (I - \Delta t L)) U(t) \\ &= (I - \Delta t L)^{-1} \Delta t (N + L) U(t) \\ &= (I - \Delta t L)^{-1} \Delta t A U(t). \end{aligned} \quad (15)$$

For Δt large,

$$B - I \approx -L^{-1} A = -L^{-1} (N + L) = -(I + L^{-1} N).$$

Similarly, the linearization of $B - I$ reduces to

$$B_U - I \approx -L^{-1} A_U = -L^{-1} (N_U + L) = -(I + L^{-1} N_U). \quad (16)$$

[Note that Δt large is the limit opposite to that for which (14) was formulated. The goal of time stepping is, roughly speaking, to approximate $e^{A \Delta t}$, which is accomplished by (14) when Δt is *small*.]

From the calculation in (15) it is clear that the roots of $B - I$ are identical to those of A , barring values of Δt such that $I - \Delta t L$ is singular. Roots of $B - I$ can be calculated by Newton's method:

$$(B_U - I)u = (B - I)U, \quad U \leftarrow U - u. \quad (17)$$

The Jacobian $B_U - I \approx I + L^{-1} N_U$ is far better conditioned than the operator $A_U = N_U + L$ appearing in (11). Multiplication by L^{-1} or an approximation to it, as in Eq. (16), acts as a preconditioner, an approximate inverse to $L + N_U$. Another way of saying this is that $L^{-1} N_U$ is, in some sense, a small perturbation to the identity. Multiplication by L^{-1} has been called *Stokes preconditioning* by Carey,¹² since L by itself is the evolution operator for Stokes flow.

We now discuss the solution of (17). An iterative conjugate-gradient solver such as NSPCG¹³ in format-free mode requires, in addition to the right-hand side $(B - I)U$, a subroutine which acts with $B_U - I$ on any vector u . Both are already essentially available within the time-stepping code. As seen in (15), $(B - I)U$ is merely the difference between velocities at two successive (very widely spaced) time steps. To evaluate $(B_U - I)u$ all that need be done is to adapt routines which calculate (4) and (5) to calculate the corresponding linearized versions (12) and (13). This method can also be implemented when the time evolution operator B uses Crank–Nicolson rather than backwards-Euler time stepping. Or L^{-1} itself can be used as a preconditioner, rather than $(I - \Delta t L)^{-1} \Delta t$, at the cost of a slight increase in programming effort. Thus, the Newton steady-state algorithm can be implemented by changing fewer than 20 lines of the time-stepping code, and without writing any new low-level code.

In the case of a symmetric positive (or negative) definite matrix, conjugate gradient iteration is a well-defined algorithm whose convergence is guaranteed. For other matrices, there exist a number of generalizations, none of which is superior or guaranteed to converge in all cases.¹⁴ Of the variants provided by the NSPCG software library,¹³ we have found that *biconjugate gradient squared* (BCGS) converges most quickly and reliably, usually in 30 to 70 steps.

D. Continuation

To follow a branch of steady solutions efficiently and, more fundamentally, to reach the “partner” of a branch connected by a saddle-node bifurcation, it is necessary to be able to carry out *continuation*.^{15,16} That is, we sometimes wish to consider the control parameter—here, the Reynolds number—as a dependent variable, while fixing another variable instead, such as one of the velocity values.

Here we will use the notation U_m to mean any one of the M quantities used to represent a flow field, i.e., one of the values of ω or ψ in either the gridspace or the spectral representation. Sufficiently close to a saddle-node bifurcation, one of the components U_m (and eventually all of them) must necessarily change faster along the branch than the Reynolds

number. When this happens, the fastest-changing U_m is set equal to a specified value U_m^* , and Re treated as a dependent variable.

We now formulate the expanded system of equations for (U, Re) and the Newton method for solving them. We rewrite our schematic representation to explicitly include the Reynolds number as in (2)–(3):

$$\frac{dU}{dt} = N(U) + \frac{1}{Re} LU.$$

If \bar{U} represents U with the restriction $U_m = U_m^*$ we may write the steady-state equations as a system of M equations in M unknowns:

$$A(\bar{U}, Re) \equiv Re N(\bar{U}) + L\bar{U} = 0.$$

As before, both for the purpose of preconditioning and for compatibility with the time-stepping code, we define the time-stepping operator

$$B(\bar{U}, Re) \equiv (I - \Delta t L)^{-1} (I + \Delta t Re N) \bar{U}$$

so that steady states are solutions to $B(\bar{U}, Re) - \bar{U} = 0$. Letting \bar{u} and re be the decrements to the current guesses for the truncated velocity \bar{U} and the Reynolds number Re , one Newton step is written:

$$\begin{aligned} (B_{\bar{U}} - I)\bar{u} + B_{Re} re &= B(\bar{U}, Re) - \bar{U}, \\ \bar{U} &\leftarrow \bar{U} - \bar{u}, \\ Re &\leftarrow Re - re, \end{aligned} \quad (18)$$

where

$$\begin{aligned} B_{\bar{U}} - I &= (I - \Delta t L)^{-1} (I + \Delta t Re N_{\bar{U}}) - I \\ &\approx -L^{-1} (Re N_{\bar{U}} + L), \\ B_{Re} &= (I - \Delta t L)^{-1} \Delta t N(\bar{U}) \approx -L^{-1} N(\bar{U}). \end{aligned}$$

Equation (18) is again solved iteratively via BCGS. To act with the linear operator on the left-hand side of (18) on u and re , while retaining as much as possible of the ordinary time-stepping routines, we expand \bar{u} by setting $u_m = 0$, act with $B_{\bar{U}} - I$ by subtracting two successive linearized time steps, and then add the vector $B_{Re} re$.

Newton solving and continuation provide a far more rapid method of calculating stable steady states than integrating in time until a stationary state is reached; calculating unstable steady states by time integration is, of course, impossible. An entire branch ($0 \leq Re \leq 2500$) can be calculated using this method in less than an hour of CPU time on a Cray YMP.

E. Linear stability analysis

The linear stability of a steady state or flow U is determined by its leading eigenvalues: those with greatest real part. However, the eigenvalues found most readily by iterative methods are the dominant ones: those with largest magnitude. The remedy is an exponential transformation: leading eigenvalues of A are dominant eigenvalues of $\exp(A)$. Since exactly exponentiating A would itself require the diagonalization we seek to accomplish, we act with an approximate

exponential instead, derived from the time-stepping code. The block power, or Arnoldi's, method is used in order to find several leading eigenvalues, including complex or multiple eigenvalues, simultaneously. This combination of methods is essentially that described by Goldhirsch, Orszag, Maulik,¹⁷ and in Christodoulou and Scriven;¹⁸ we summarize our adaptation of it below.

Using the notation of the previous sections, the equations governing the evolution of an infinitesimal perturbation u to U can be abbreviated as

$$\frac{du}{dt} = N_U u + L u = A_U u. \quad (19)$$

Replacing N by N_U in either of (7)–(8) or (14), as before, results in a time-stepping operator B_U for (19). For simplicity of exposition, we discuss Euler time stepping for which

$$\begin{aligned} B_U &= (I - \Delta t L)^{-1} (I + \Delta t N_U) \\ &\approx \exp(A_U \Delta t) \quad \text{for } \Delta t \text{ small.} \end{aligned} \quad (20)$$

Based on (20), the eigenvectors of A_U and B_U are approximately (to order Δt) the same, while their eigenvalues are related by

$$\lambda(A_U) \approx \frac{1}{\Delta t} \log \lambda(B_U).$$

To estimate the K leading eigenvectors and eigenvalues of A_U , we integrate (19) for some fairly long period of time T , or equivalently, act repeatedly with B_U on some initial vector. The effect of this is to purge the vector of the most quickly decaying eigenvectors, yielding a vector containing primarily the leading eigenvectors. We then take K additional time steps, creating vectors $u_1 = u(T), u_2 = u(T + \Delta t), \dots, u_{K+1} = u(T + K\Delta t)$. Each vector u_k is orthogonalized to those previously generated, yielding a vector w_k , and then normalized to yield another vector v_k . The space spanned by the first K of these, $\{v_1, \dots, v_K\}$, is called the Krylov subspace.

The vectors v_k can be assembled into an $N \times K$ matrix V , and the inner products $\langle v_j, B_U v_k \rangle$, which are generated as a by-product of the orthonormalization procedure, into a $K \times K$ matrix H . This procedure is described formally by the *Arnoldi equation*:

$$B_U V - V H = w_{K+1} e_K^T$$

where e_K is the K th unit vector. Thus, the Arnoldi procedure is successful—i.e., the action of B_U on the subspace spanned by the v_k 's is well approximated by H —insofar as w_{K+1} is small. More details may be found in Refs. 19–21.

This small matrix H is diagonalized, yielding eigenvalues λ and eigenvectors Ψ . Approximate eigenpairs of the large matrix B_U are λ and $V\Psi$ as is shown by the following:

$$\begin{aligned} \|(B_U - \lambda)(V\Psi)\|^2 &= \|B_U V\Psi - V H\Psi\|^2 \\ &= \|w_{K+1} e_K^T \Psi\|^2 \\ &= \|w_{K+1}\|^2 |e_K^T \Psi|^2 \end{aligned} \quad (21)$$

where (21) gives the error in each approximate eigenpair. If the required number of eigenpairs has not been calculated to

Steady Vortex States

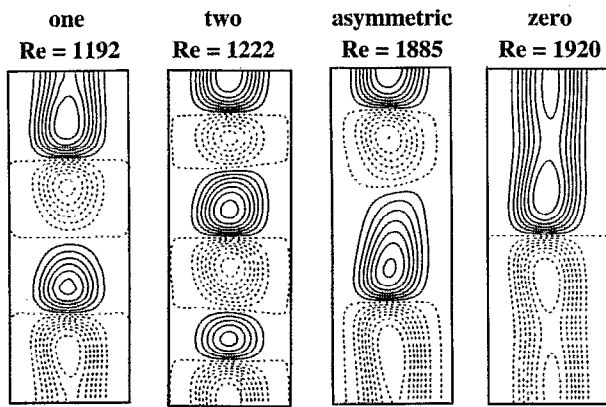


FIG. 1. Steady flows. Contours of the meridional streamfunction are shown. Counter-clockwise circulation is shown as solid curves, clockwise circulation as dashed curves. The region shown, $r_1 \leq r \leq r_2$, $3\pi/8 \leq \theta \leq 5\pi/8$, is actually curved, although it is depicted here as rectangular for simplicity. Shown are a one-vortex state at $Re=1192$, a two-vortex state at $Re=1222$, an asymmetric one-vortex state at $Re=1885$, and a supercritical zero-vortex state at $Re=1920$. The one-vortex and asymmetric states have weak inflow boundaries at or near the equator, while the two- and zero-vortex states have strong outflow at the equator.

the desired accuracy, the process may be repeated, by time-integrating (19) for another period T beginning from the vector u_1 .

In practice, we find that $K=4$ works well for obtaining the two converged eigenvectors that our bifurcation analysis will require. When computing parity-breaking bifurcations, K can be taken even smaller, since eigenvectors of both parities can be calculated simultaneously as a single eigenvector.

III. RESULTS

A. Stable flows and transitions between them

Figure 1 depicts the flows studied in this article. For simplicity, we represent the domain as rectangular, although it is actually curved. We show only the region of interest $3\pi/8 \leq \theta \leq 5\pi/8$, a subset of the domain of calculation $0 \leq \theta \leq \pi$. Contours of $\psi r \sin \theta$ are plotted; these are tangent to the meridional velocity, as shown by (1). The solid curves designate counter-clockwise circulation, and the dashed curves designate clockwise circulation. As in cylindrical Taylor-Couette flow, there also exists a much larger azimuthal velocity component, which is not shown here.

Ekman pumping at the poles causes large-scale meridional flow whose direction is counter-clockwise in the northern hemisphere, and clockwise in the southern hemisphere. This large-scale circulation is present at all nonzero Reynolds numbers; its edges are visible on the upper and lower parts of each of the flows depicted.

The first state shown in Fig. 1 is a one-vortex state at $Re=1192$. Each hemisphere contains one Taylor vortex. These are separated at the equator by a relatively weak inflow boundary, which differs markedly from the two strong outflow boundaries that separate the vortices from the large-scale meridional flow. Strong outflow and weak inflow

One- to Two- Vortex Transition at $Re = 1193$

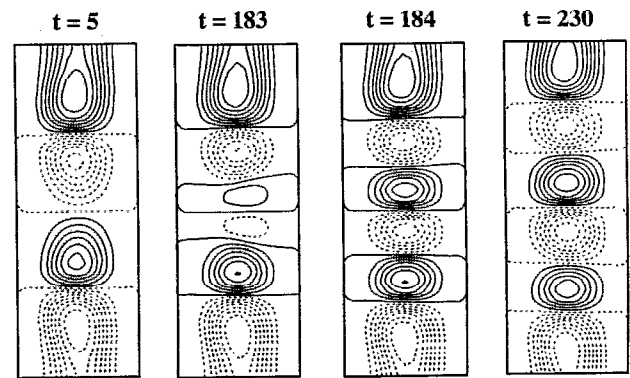


FIG. 2. Transition from one-vortex to two-vortex state. The initial condition is a one-vortex state at $Re=1190$; at $t=0$, Re is suddenly increased to 1193. The same transition takes place whenever Re is increased from values below 1192 to values within the range $1192 < Re < 1244$.

boundaries are a typical feature of Taylor-vortex flow in both spherical and cylindrical geometries.^{1,5,22} The next state depicted is a two-vortex state at $Re=1222$. Each hemisphere contains two Taylor vortices and the equator is a strong outflow boundary. The asymmetric one-vortex state shown at $Re=1885$ has a larger “southern” vortex, but the other symmetrically related state can be created as well. Throughout the remainder of this article, we will refer to an asymmetric one-vortex state merely as an asymmetric state; the nomenclature zero-, one-, and two-vortex states will always refer to symmetric states.

The one- and two-vortex states depicted in Fig. 1 can be obtained via time-integration by adiabatically increasing Re from 0. However, the asymmetric one-vortex state cannot be obtained in this way. Instead, we followed the procedure suggested by Bühler.¹ This “recipe” requires, first, a sudden acceleration from rest to $Re=1920$. This yields the zero-vortex state also depicted in Fig. 1, termed the *supercritical* zero-vortex state² to differentiate it from zero-vortex states obtained by adiabatically increasing Re from 0. The asymmetric one-vortex state is then obtained by decreasing Re . The necessity for this procedure can be understood from the bifurcation diagram presented in Sec. III B.

We now describe the transitions observed using time-integration. The procedure is to begin with a stable steady state at some Reynolds number, set the Reynolds number to some other value, and time-integrate until a new stable steady state is reached. In our discussion of transitions, times are given in terms of revolutions of the inner sphere.

Figure 2 depicts the transition from the one-vortex state to the two-vortex state which occurs when Re is increased from 1191 to 1193. An initially very small pair of vortices is created at the weak inflow boundary separating the two pre-existing equatorial vortices. The new vortices grow and displace the pre-existing vortices. This transition is essentially identical to that observed by Bühler in increasing Re from 1250 to 1300. We have verified that the same transition occurs when Re is increased in smaller steps, and the flow allowed to equilibrate after each increase, or when Re is

Asymmetric- to Two- Vortex Transition at $Re = 1222$

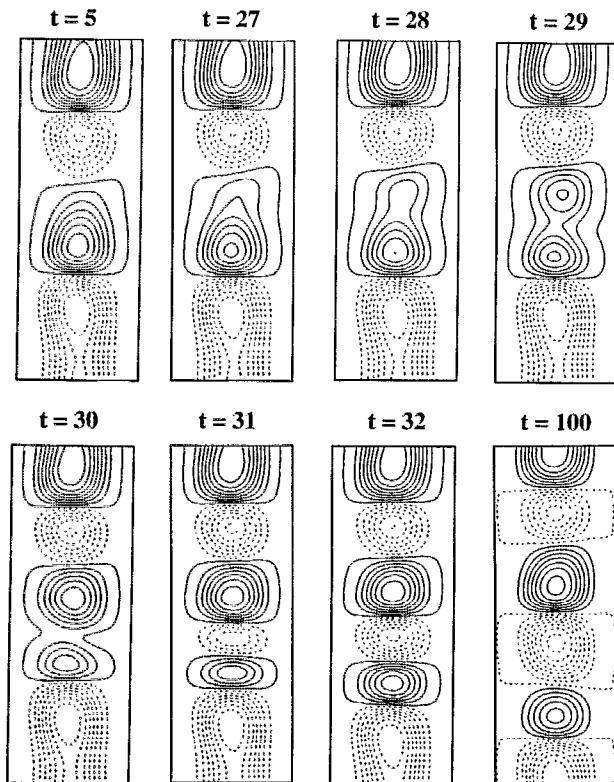


FIG. 3. Transition from asymmetric to two-vortex state. The initial condition is an asymmetric state at $Re=1250$; at $t=0$, Re is suddenly decreased to 1222. The same transition takes place whenever Re is decreased from values above 1244 to values within the range $1192 < Re < 1244$.

increased to any value within the range $1193 < Re < 1244$.

Figure 3 shows the transition from the asymmetric state to the two-vortex state which takes place when Re is decreased from 1245 to 1222. A stagnation point first appears within the larger, southern vortex at approximately $t=28$. Afterwards, regions of counter-rotating circulation appear near the sidewalls, at approximately the same latitude as the stagnation point. When these join, they form a narrow counter-rotating vortex that divides the former southern vortex into two. The narrow vortex expands and the flow eventually becomes symmetric. A theory proposed by Dumas²³ concerning Taylor-vortex formation predicts that stagnation points could form within elongated Taylor vortices, thereby leading to the pinching off of additional vortices just as occurs in Fig. 3.

This transition from the asymmetric to the two-vortex state contradicts Bühler's observation of a transition from the asymmetric to the *one-vortex* state when he decreased Re abruptly from 1300 to 1200. We reproduced his transition, but only by decreasing Re abruptly to below 1193. Transition to the two-vortex state occurs whenever the initial condition is an asymmetric state and Re is decreased from values above 1244 to values within the range $1193 < Re < 1244$. The two-vortex state persists when Re is further decreased to val-

Supercritical-Zero to Asymmetric Transition at $Re = 1885$

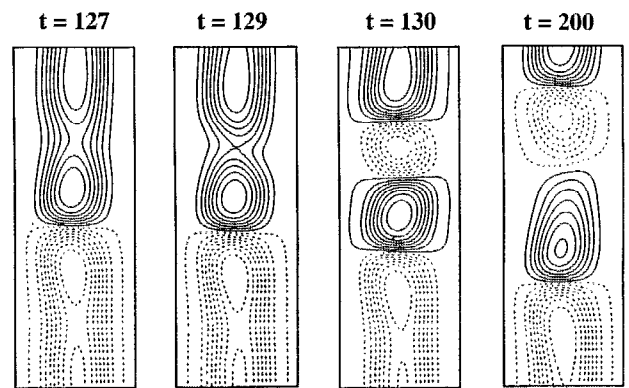


FIG. 4. Transition from supercritical zero-vortex state to asymmetric state. The initial condition is a supercritical zero-vortex state at $Re=1925$; at $t=0$, Re is suddenly decreased to 1885.

ues below 1193. Thus, $1193 < Re < 1244$ is a "window" for transition to the two-vortex state from either the one-vortex or the asymmetric state. The explanation for this window will be given in the next section.

Figure 4 depicts the transition from the supercritical zero-vortex state to the asymmetric one-vortex state that occurs when Re is decreased from 1925 to 1885. The streamlines of the counter-clockwise, northern hemisphere become "pinched" at the latitude of their stagnation point. This permits regions of clockwise circulation to form near the two radial walls. Eventually, these regions join, forming a single clockwise vortex which divides the counter-clockwise region in two. Both new vortices grow, with the counter-clockwise vortex surpassing the clockwise vortex. This transition could also start off in the southern hemisphere, leading to an asymmetric state with a larger clockwise vortex.

B. Unstable steady states and bifurcation diagram

We have used our steady-state/continuation code to compute branches of all the solutions described in the preceding section. Figure 5 summarizes the states, stable and unstable, that we have calculated in the range $600 \leq Re \leq 1400$. Each steady flow is represented by the torque τ it exerts on the outer sphere.

As a bifurcation diagram, the representation of τ vs Re is flawed. Figure 5 contains many crossings between the various curves, most of which do not represent bifurcations: two states at an intersection point are generally not identical, but merely have the same torque. In addition, the bifurcations which do occur are generally grouped too closely together in Re to be easily distinguished in the figure. For these reasons, we have also provided a schematic representation of the bifurcation diagram in Fig. 6. In order to avoid intersections, the vertical ("schematic") axis of Fig. 6 is not a monotonic—nor even a single-valued—function of torque.

We find it useful to indicate for each branch the number and parity of the eigenvectors to which it is unstable. A stable branch will be labeled with its "instability index"²⁴ i

TORQUE VERSUS REYNOLDS NUMBER

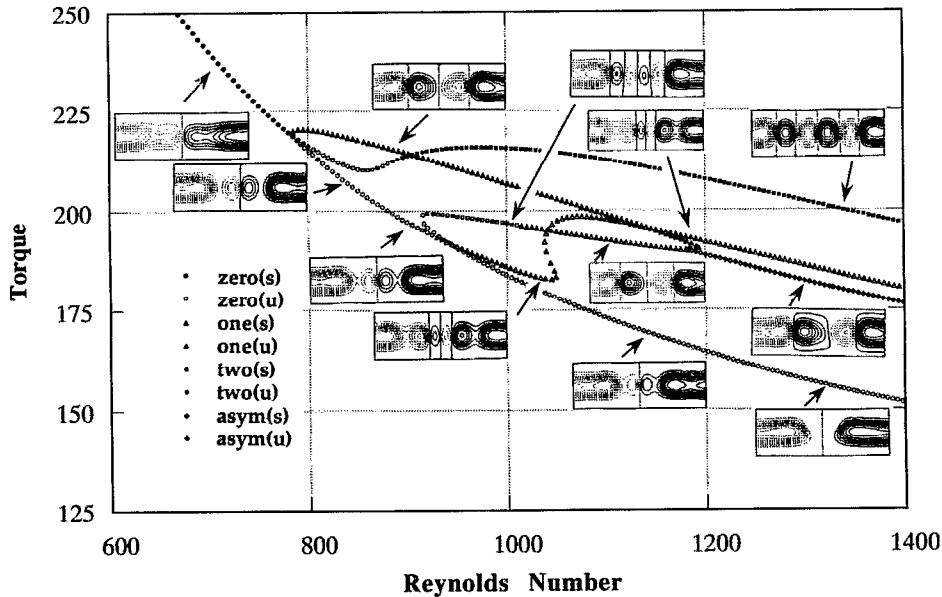


FIG. 5. Torque vs Re for the range $600 \leq \text{Re} \leq 1400$. Corresponding flows (zero-, one-, two-vortex or asymmetric; stable or unstable) are shown as insets.

of 0. For a symmetric state, each eigenvector is necessarily either symmetric or antisymmetric, so an unstable symmetric branch will be labeled with an index of s if it has one symmetric unstable eigenvector, of a if it has one antisymmetric unstable eigenvector, and of sa if it has one eigenvector of each parity. The eigenvectors of an *asymmetric* state have no definite parity, so unstable asymmetric branches will be labeled with an instability index of 1, 2, ..., indicating one or more unstable eigenvectors.

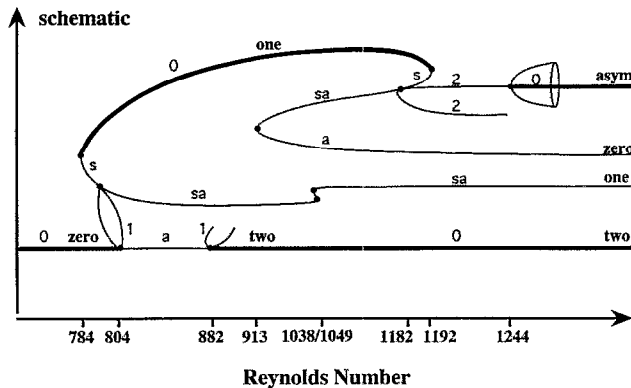


FIG. 6. Schematic bifurcation diagram for $\text{Re} \leq 1400$. The flows corresponding to each branch are labeled as **zero**, **one**, **two**, or **asym**. Each branch is labeled with its instability index, i.e., the number of eigenvectors (0, 1, or 2) to which it is unstable. Symmetric states have eigenvectors of definite parity and are instead labeled as s (symmetric), a (antisymmetric), or sa (one of each). For emphasis, stable states are denoted by bold curves. Note that the branches are not ordered by torque. A sequence of closely related transitions results from the saddle-node bifurcation at $\text{Re}=784$ and subcritical pitchfork bifurcations at $\text{Re}=804, 882$. Another sequence of transitions results from the subcritical pitchfork bifurcation at $\text{Re}=1182$, the saddle-node bifurcation at $\text{Re}=1192$, and the subcritical Hopf bifurcation at $\text{Re}=1244$.

We see from Figs. 5 and 6 and from previous work^{25,26,4,5} that one-vortex states originate in a saddle-node bifurcation at $\text{Re}=784$ where a pair of branches, one stable (index 0) and one unstable (index s), is created. The fate of the unstable branch is quite complicated. Very close to the saddle-node it undergoes a supercritical symmetry-breaking pitchfork bifurcation⁶ increasing its instability index from s to sa . The unstable (index 1) asymmetric branches thus created disappear shortly thereafter at $\text{Re}=804$, via a crucial subcritical pitchfork bifurcation which destabilizes the zero-vortex branch (increasing its index from 0 to a) and is responsible for the initial formation of Taylor vortices.⁴⁻⁷ The states on the zero-vortex branch gradually become two-vortex states,⁵ and the branch restabilizes via another pitchfork bifurcation.

We now follow the stable one-vortex branch up to and around its turning point (saddle-node bifurcation) at $\text{Re}=1192$, where its index increases from 0 to s . The branch undergoes a subcritical pitchfork bifurcation at $\text{Re}=1182$, causing its index to increase further to sa , and then undergoes another saddle-node bifurcation at $\text{Re}=913$, decreasing its index to a . Along the way, the states along this unstable branch become two-vortex states and finally zero-vortex states, as can be seen in the insets of Fig. 5.

Symmetric and antisymmetric eigenvectors of the one-vortex state at the turning point at $\text{Re}=1192$ are shown in Fig. 7. Their appearance is typical of eigenvectors all along the branch. The symmetric eigenvector in Fig. 7 is associated with the turning point, and so has eigenvalue 0 at this point. The antisymmetric eigenvector in Fig. 7 is responsible for the subcritical pitchfork bifurcation at $\text{Re}=1182$, and so at the nearby turning point its eigenvalue is small: $\lambda = -0.0185\Omega$.

States on the branches created at the pitchfork bifurca-

Eigenvectors of One-Vortex State at $Re = 1192$

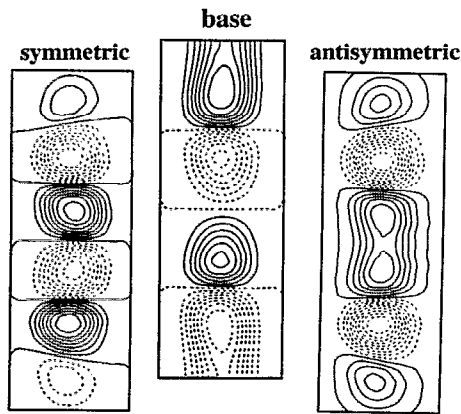


FIG. 7. Eigenvectors. The two most unstable eigenvectors associated with the one-vortex state (labeled "base") undergoing a saddle-node bifurcation at $Re=1192$. The eigenvalues associated with the symmetric and antisymmetric eigenvectors at this point are 0 and -0.0185Ω , respectively.

tion at $Re=1182$ are asymmetric, and their asymmetry increases along the branches. These new branches bifurcate subcritically, meaning that they inherit the stability index of the *less stable* portion of the parent branch. We use the definition of subcriticality found, e.g., in Ref. 24: here, this means that the asymmetric branches are created with two unstable eigenvectors, and they bifurcate towards increasing Re .

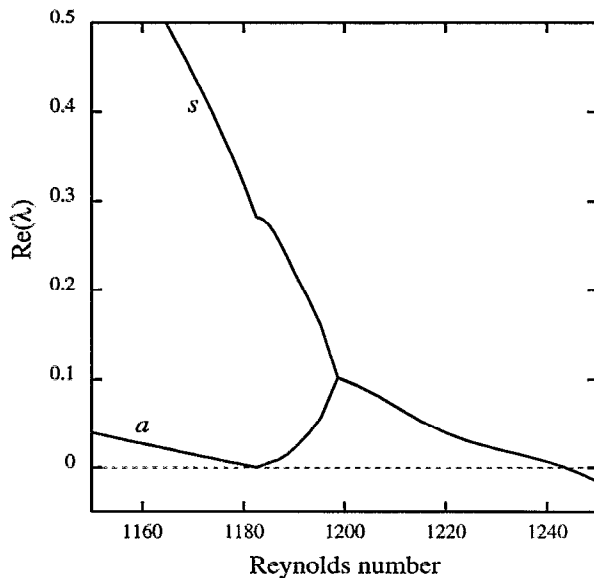


FIG. 8. Eigenvalues. The two most unstable eigenvalues as a function of Re along a path leading to the asymmetric branch. For $1150 \leq Re \leq 1182$ the base state is a one-vortex state with two positive eigenvalues, associated with a symmetric (s) and an antisymmetric (a) eigenvector resembling those of Fig. 7. We switch branches at $Re=1182$ (subcritical pitchfork bifurcation), where the a eigenvalue is 0, leading to a discontinuity in the first derivative. For $1182 \leq Re \leq 1250$, the base state followed is an asymmetric state. At $Re=1197$, the two eigenvalues join to form a complex conjugate pair whose real part crosses zero at $Re=1244$ (subcritical Hopf bifurcation).

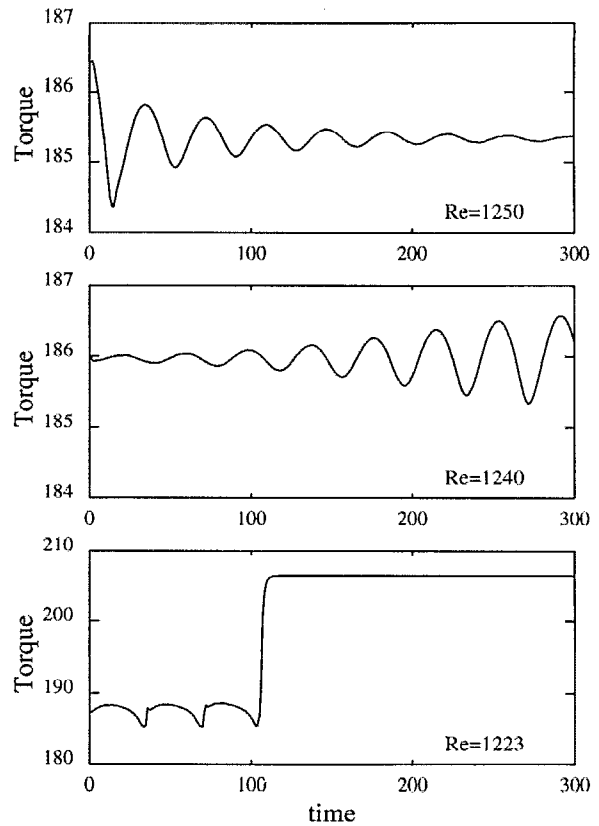


FIG. 9. Torque vs time. Initial conditions are asymmetric states at Re slightly above 1250. Top: damped oscillations when Re is decreased to 1250. Middle: growing oscillations when Re is decreased to 1240, just below Hopf bifurcation at $Re=1244$. Bottom: abrupt oscillations culminating in transition to a two-vortex state when Re is decreased to 1223.

For each asymmetric branch to become stable, both of its positive eigenvalues must change sign. Figure 8 displays these two eigenvalues as a function of Re . Between $Re = 1150$ and $Re=1182$, we plot the eigenvalues of the unstable (sa) one-vortex branch. (The corresponding eigenvectors resemble those of Fig. 7.) At the bifurcation at $Re = 1182$, where the antisymmetric eigenvalue is 0, we switch to following the eigenvalues of the new asymmetric branches, labeled 2 in Fig. 6. This branch-switching causes the curves of Fig. 8 to be continuous but not smooth at 1182. The two unstable eigenvalues coalesce to form a complex-conjugate pair at $Re=1197$. The real part of the eigenvalue pair decreases, eventually changing sign at $Re=1244$ in a Hopf bifurcation. Both asymmetric branches are subsequently stable, and thus labeled 0 in Fig. 6.

The Hopf bifurcation is confirmed and shown to be subcritical by time-dependent integration. In Fig. 9 we present time series of the torque taken in the vicinity of the Hopf bifurcation. The initial conditions are asymmetric states at Re slightly above 1250. When the Reynolds number is lowered abruptly to 1250, damped oscillations are seen as the flow adjusts to the lower Reynolds number. At $Re=1240$, just below the Hopf bifurcation at $Re=1244$, the torque undergoes growing oscillations. At $Re=1223$, a sequence of abrupt, highly anharmonic oscillations culminates in a transition to the two-vortex state.

TORQUE VERSUS REYNOLDS NUMBER

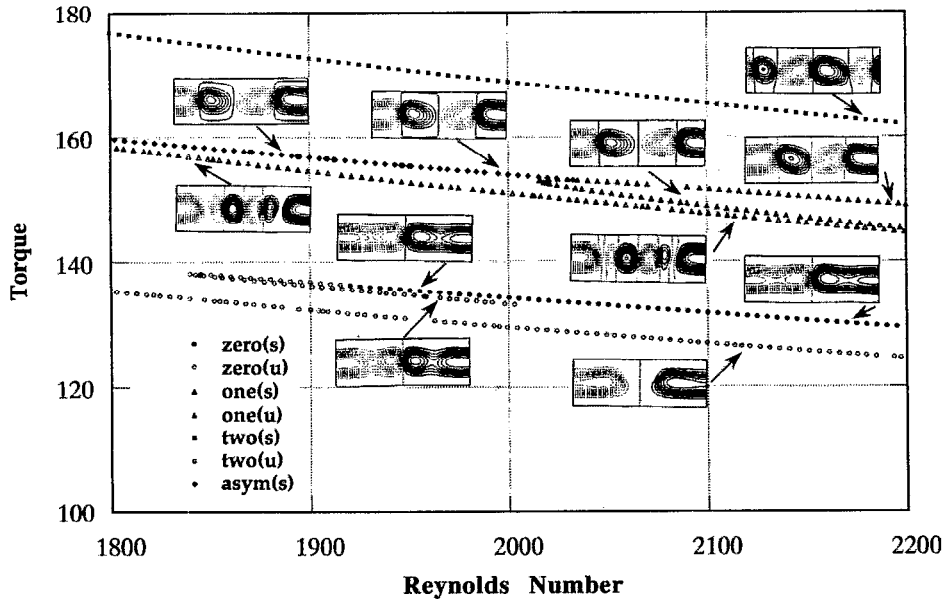


FIG. 10. Torque vs Re for the range $1800 \leq Re \leq 2200$. Corresponding flows (zero-, one-, two- vortex or asymmetric; stable or unstable) are shown as insets.

This Hopf bifurcation is, to our knowledge, the first to be computed in spherical Couette flow. Note that this Hopf bifurcation is not of the type associated with the breaking of axisymmetry and the onset of rotating waves; there is no reference frame in which the periodic orbit created is seen as a steady state.

C. Higher Reynolds numbers

Figures 10 and 11 show steady flows existing in the range $1800 \leq Re \leq 2200$. These were computed using 32 gridpoints in r and 256 gridpoints in θ , double the resolution

used in the lower Reynolds number range. Figure 10, like Fig. 5, represents each state by its torque. Figure 11 is a schematic rendering, whose vertical axis, unlike that of Fig. 6, preserves the ordering in torque. The branches at the left of Figs. 10 and 11 are continuations of those at the right of Figs. 5 and 6. The stable two-vortex branch and the unstable zero (a) and one (sa) vortex branches undergo no qualitative changes in this range of Reynolds number.

A pair of new zero-vortex branches are created at $Re = 1839$ by a saddle-node bifurcation. Although both are initially unstable (indices a and sa), the more stable (a) of the branches is stabilized by a subcritical pitchfork bifurcation at $Re = 1920$. The resulting stable zero-vortex branch is observable in experiments^{1,2} and in time-dependent simulations¹ as what is called the supercritical zero-vortex state. Symmetric and antisymmetric eigenvectors of the supercritical zero-vortex state at $Re = 1920$ are shown in Fig. 12.

Schrauf⁷ computed bifurcations of the same type—a saddle-node bifurcation of zero-vortex branches and a subcritical pitchfork bifurcation from one of these zero-vortex branches—for a variety of gap sizes. Extrapolating from his data to our gap size of $\sigma = 0.154$, both bifurcations would occur at around $Re = 2000$, in accordance with our computations. Especially interesting is the coalescence Schrauf displays in the (Re, σ) plane between this pitchfork bifurcation of a zero-vortex branch and that which occurs at low Reynolds number (see Fig. 6, $Re = 804$). This implies that the low and high Reynolds number zero-vortex branches are themselves connected in some way for $\sigma > 0.23$.

The upper part of Fig. 11 shows the stable asymmetric branches terminating in a pitchfork bifurcation at $Re = 2034$. This bifurcation is supercritical, since the bifurcating asymmetric branches inherit the stability of the more stable (index 0) portion of the parent branch. Here, the parent branch is

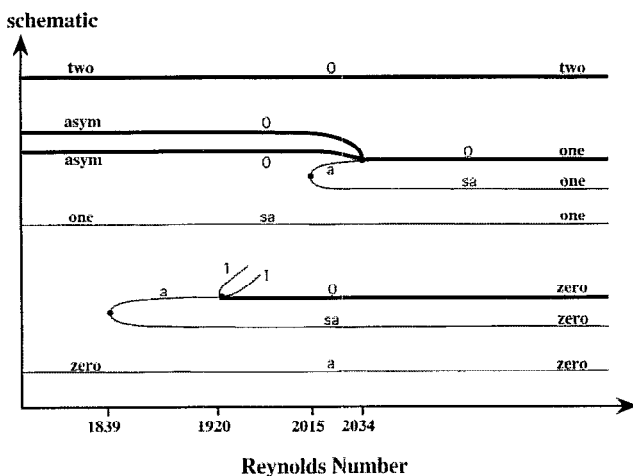


FIG. 11. Schematic bifurcation diagram for $1800 \leq Re \leq 2200$. Conventions as in Fig. 6. The important features are the saddle-node bifurcations at $Re = 1839$ and $Re = 2015$ and the pitchfork bifurcations at $Re = 1920$ and $Re = 2034$. Here, the “schematic” variable is a monotonic function of torque.

Eigenvectors of Zero-Vortex State at $Re = 1920$

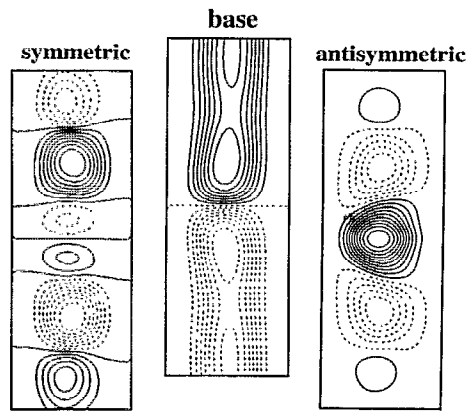


FIG. 12. Eigenvectors. Base state is supercritical zero-vortex state at $Re = 1920$. The symmetric eigenvector is associated with the saddle-node bifurcation at $Re = 1839$, the antisymmetric eigenvector with the subcritical pitchfork bifurcation at $Re = 1920$.

one of a pair of one-vortex branches created by a saddle-node bifurcation at $Re = 2015$. This part of Fig. 11 should be viewed as somewhat conjectural. In particular, according to the scenario that we have just described, transition between the stable asymmetric and one-vortex branches should take place without hysteresis at $Re = 2034$. This is in accordance with some *experimental* observations by Böhler.¹ However, time-dependent computations by Böhler and by us produced a transition from the one- to the *two*-vortex (rather than asymmetric) state when Re was decreased. We have not been able to perform computations at sufficiently small intervals in Re to resolve this inconsistency.

The bifurcations at $Re = 1192$ and $Re = 2034$ which we have calculated for $\sigma = 0.154$ delimit a range of non-existence for the stable one-vortex state, a result which is confirmed experimentally.¹ We should point out that this result depends sensitively on σ . For slightly larger gap widths ($\sigma = 0.176$ or $\sigma = 0.18$), it is well established^{1,4-6} that a continuous stable one-vortex branch exists, rather than two disconnected branches. However, a nonexistence range can easily be erroneously produced either numerically^{6,26} or experimentally,² thus indicating the “fragility” of the solutions to the Navier–Stokes equations in this region of (Re, σ) .

IV. DISCUSSION

We have demonstrated the feasibility of a unified computational approach that combines time integration, steady-state solving, and linear stability analysis to determine the bifurcation structure of hydrodynamic problems. At the heart of our approach is the discovery that the difference between two very widely spaced time steps can be used to calculate stable and unstable steady states via Newton’s method, and that the implicit viscous step already implemented in the time-stepping code serves as a very effective preconditioner. A pre-existing time-dependent code can thus be modified

through relatively minor, high-level changes, to also carry out steady-state solving and linear stability analysis.

We have used this comprehensive computational framework to unravel the rather complicated scenario connecting the one-vortex state with its asymmetric cousins in a medium-gap spherical Couette flow. A total of three bifurcations are involved: (1) a saddle-node at $Re = 1192$ from the stable to the unstable portions of the one-vortex state, (2) a subcritical pitchfork at $Re = 1182$, leading to the formation of the unstable asymmetric branches, and (3) a subcritical Hopf bifurcation at $Re = 1244$, stabilizing the asymmetric branches.

We have also calculated bifurcations at higher Reynolds numbers via which the asymmetric branches die and a branch of supercritical zero-vortex states is born. Both of these events combine turning points and symmetry-breaking pitchfork bifurcations.

Bifurcation scenarios very similar to the one we have calculated in the vicinity of $Re = 1200$ have been observed both experimentally and numerically by Mullin, Cliffe, and Pfister²⁷ and by Tavener, Mullin, and Cliffe²⁸ in Taylor–Couette flow between short cylinders [$3.2 < L/(r_2 - r_1) < 5.6$, where L is the length of the cylinders]. These authors interpret this sequence of bifurcations as the unfolding of a codimension-two bifurcation in which the pitchfork and saddle-node coincide. Guckenheimer^{29,30} and Knobloch and Moore³¹ discuss the qualitative behavior near this bifurcation, whose normal form is given by

$$\partial_t a = a(\epsilon + cs) + O(3), \quad (22)$$

$$\partial_t s = \mu - s^2 + a^2 + O(3). \quad (23)$$

The correspondence between (22)–(23) and the Taylor–Couette problem is as follows: a and s are the amplitudes of antisymmetric and symmetric modes, respectively, and μ is related to the Reynolds number; ϵ is an additional control parameter, i.e., aspect ratio or gap width, which serves to bring the saddle-node and pitchfork bifurcations together. The dynamics described by (22) and (23) are illustrated in Fig. 13. In the systems studied by Mullin *et al.*²⁷ and by Tavener *et al.*,²⁸ the Hopf bifurcations are supercritical and the resulting stable axisymmetric periodic orbits can be observed and studied.

Certainly, asymmetry and time-dependence are closely linked. For symmetric states, it has been observed, both here and in earlier work (see Ref. 32 and references in Ref. 5) on spherical and finite-length cylindrical Taylor–Couette flow, that eigenvalues of symmetric and antisymmetric eigenvectors tend to be interleaved. We attribute this to the near-degeneracy of symmetric and antisymmetric eigenvectors derived from the translational symmetry of the infinite-length cylindrical case. As long as the eigenvalues remain interleaved, they cannot become complex, since eigenvectors of opposite parity cannot coalesce. Their eigenvalues can, however, cross one another, freeing the same-parity eigenvectors to coalesce into complex-conjugate pairs. This is one way in which eigenvectors may become complex. The second way is the one we have computed here: the underlying steady states become asymmetric, coupling the eigenvectors that

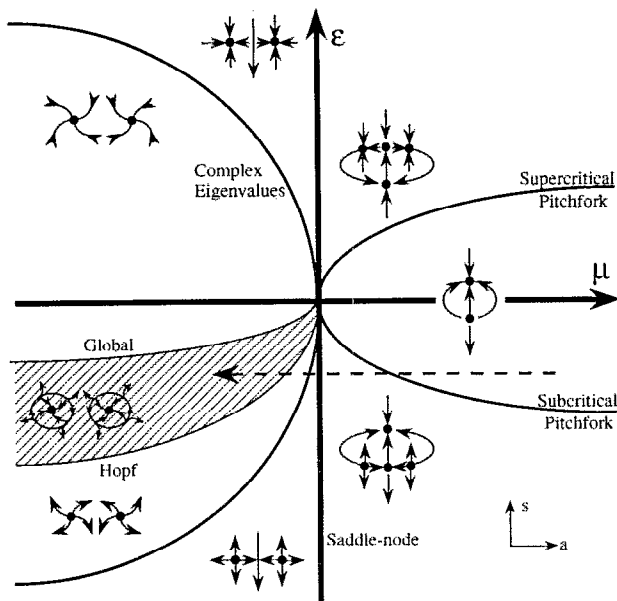


FIG. 13. Unfolding of simultaneous saddle-node and pitchfork bifurcations described by normal form (22)–(23) with $-1/2 < c < 0$. In each region of the (μ, ϵ) plane are shown phase portraits depicting dynamics in the symmetric (s) and antisymmetric (a) directions. Symmetric steady states are created and destroyed by saddle-node bifurcations along $\mu=0$, asymmetric states by pitchfork bifurcations at $\mu=(\epsilon/c)^2$. The Hopf and global bifurcations that create and destroy the limit cycles in the hatched region require cubic terms. The dashed path corresponds to the scenario observed in spherical Couette flow when increasing Re from below 1182 to above 1244 (see Fig. 6).

were formerly of opposite parity. Both ways require broken translational symmetry: either boundary conditions are imposed by the endplates of finite cylinders, or sphericity perturbs a fictitious translational symmetry in latitude, reducing the symmetry group from $O(2)$ to Z_2 .³³

Various hydrodynamic mechanisms, such as those proposed by Dumas,²³ may govern the types of transitions allowed. Examples of the kinds of questions raised are: When do transitions occur via formation of a stagnation point within a region of same-sign circulation (e.g., Figs. 3 and 4), and when are vortex pairs created at inflow boundaries (e.g., Fig. 2)? Can a new vortex pair ever form at an outflow boundary?⁵ Which transitions are reversible in time? What are the differences between the allowed evolution of states along a branch and in time? What physical features distinguish stable from unstable steady states? These types of investigations are usually carried out quite separately from a study of the bifurcations, and by different communities. Yet, it could prove fruitful to try to relate the bifurcation diagrams to hydrodynamics. Study of the bifurcation diagrams may suggest rules governing physical processes; conversely, hydrodynamic mechanisms may provide explanations for the complexity of the bifurcation diagrams.

ACKNOWLEDGMENTS

This study was supported by NSF Grant No. DMS-9113142. Computations were performed on the Cray YMP of

the University of Texas Center for High Performance Computing. We thank Fareed I. Siddiqui, Dwight Barkley, and John Guckenheimer for their assistance.

- ¹K. Bühler, "Symmetric and asymmetric Taylor vortex flow in spherical gaps," *Acta Mech.* **81**, 3 (1990).
- ²M. Wimmer, "Experiments on a viscous fluid flow between concentric rotating spheres," *J. Fluid Mech.* **78**, 317 (1976).
- ³I. M. Yavorskaya, Yu. N. Belyaev, A. A. Monakhov, N. M. Astaf'eva, S. A. Scherbakov, and N. D. Vvedenskaya, "Stability, non-uniqueness and transition to turbulence in the flow between two rotating spheres," in *Theoretical and Applied Mechanics*, edited by F. P. J. Rimrott and B. Tabarrok (North-Holland, Amsterdam, 1980), p. 431.
- ⁴L. S. Tuckerman, "Formation of Taylor vortices in spherical Couette Flow," Ph.D. thesis, Massachusetts Institute of Technology, 1983.
- ⁵P. S. Marcus and L. S. Tuckerman, "Numerical simulation of spherical Couette flow. Part 2. Transitions," *J. Fluid Mech.* **185**, 31 (1987).
- ⁶G. Schrauf and E. Krause, "Symmetric and asymmetric Taylor vortices in a spherical gap," in *Proceedings of the 2nd IUTAM Symposium on Laminar-Turbulent Transition*, edited by V. V. Kozlov (Springer, New York, 1985), p. 659.
- ⁷G. Schrauf, "The first instability in spherical Taylor-Couette flow," *J. Fluid Mech.* **166**, 287 (1986).
- ⁸P. S. Marcus and L. S. Tuckerman, "Numerical simulation of spherical Couette flow. Part I: Numerical methods and steady states," *J. Fluid Mech.* **185**, 1 (1987).
- ⁹D. Gottlieb and S. A. Orszag, *Numerical Analysis of Spectral Methods: Theory and Applications* (SIAM, Philadelphia, 1977).
- ¹⁰L. S. Tuckerman, "Steady-state solving via Stokes preconditioning; recursion relations for elliptic operators," in *Lecture Notes in Physics: Proceedings of the 11th International Conference on Numerical Methods in Fluid Dynamics*, edited by D. L. Dwoyer, M. Y. Hussaini, and R. G. Voigt (Springer, New York, 1989), p. 573.
- ¹¹L. S. Tuckerman, "Transformations of matrices into banded form," *J. Comput. Phys.* **84**, 360 (1989).
- ¹²G. Carey (private communication, 1988).
- ¹³D. R. Kincaid, T. C. Oppe, and W. D. Joubert, "An overview of NSPCG: A nonsymmetric preconditioned conjugate gradient package," Center for Numerical Analysis Technical Report CNA-228, Austin, Texas, 1988.
- ¹⁴N. M. Nachtigal, S. C. Reddy, and L. N. Trefethen, "How fast are nonsymmetric matrix iterations?" *SIAM J. Matrix Anal. Appl.* **13**, 778 (1992).
- ¹⁵H. B. Keller, "Numerical solution of bifurcation and nonlinear eigenvalue problems," in *Applications of Bifurcation Theory*, edited by P. H. Rabinowitz (Academic Press, New York, 1977), p. 359.
- ¹⁶R. Seydel, *From Equilibrium to Chaos: Practical Bifurcation and Stability Analysis* (Elsevier, New York, 1988).
- ¹⁷I. Goldhirsch, S. A. Orszag, and B. K. Maulik, "An efficient method for computing leading eigenvalues and eigenvectors of large asymmetric matrices," *J. Sci. Comput.* **2**, 33 (1987).
- ¹⁸K. N. Christodoulou and L. E. Scriven, "Finding leading modes of a viscous free surface flow: An asymmetric generalized eigenproblem," *J. Sci. Comput.* **3**, 355 (1988).
- ¹⁹W. E. Arnoldi, "The principle of minimized iterations in the solution of the matrix eigenvalue problem," *Q. Appl. Math.* **9**, 17 (1951).
- ²⁰Y. Saad, "Variations on Arnoldi's method for computing eigenvalues of large unsymmetric matrices," *Linear Algebra Appl.* **34**, 269 (1980).
- ²¹W. S. Edwards, L. S. Tuckerman, R. A. Friesner, and D. C. Sorensen, "Krylov methods of the incompressible Navier-Stokes equations," *J. Comput. Phys.* **110**, 82 (1994).
- ²²P. S. Marcus, "Simulation of Taylor-Couette flow. Part 2. Numerical results for wavy-vortex flow with one travelling wave," *J. Fluid Mech.* **146**, 65 (1984).
- ²³G. Dumas, "Study of spherical Couette flow via 3-D spectral simulations: Large and narrow-gap flows and their transitions," Ph.D. thesis, California Institute of Technology, 1991.
- ²⁴L. S. Tuckerman and D. Barkley, "Bifurcation analysis of the Eckhaus instability," *Physica D* **46**, 57 (1990).
- ²⁵G. Schrauf, "Branching of Navier-Stokes equations in a spherical gap," in *Lecture Notes in Physics: Proceedings of the 8th International Conference on Numerical Methods in Fluid Dynamics*, edited by E. Krause (Springer, New York, 1982), p. 474.

- ²⁶G. Schrauf, "Lösungen der Navier-Stokes Gleichungen für stationäre Strömungen im Kugelspalt," Ph.D thesis, Universität Bonn, 1983.
- ²⁷T. Mullin, K. A. Cliffe and G. Pfister, "Unusual time-dependent phenomena in Taylor-Couette flow at moderately low Reynolds numbers," *Phys. Rev. Lett.* **58**, 2212 (1987).
- ²⁸S. J. Tavener, T. Mullin, and K. A. Cliffe, "Novel bifurcation phenomena in a rotating annulus," *J. Fluid Mech.* **229**, 483 (1991).
- ²⁹J. Guckenheimer, "Multiple bifurcation problems of codimension two," *SIAM J. Math. Anal.* **15**, 1 (1984).
- ³⁰J. Guckenheimer, "On a codimension two bifurcation," in *Lecture Notes in Mathematics: Dynamical Systems and Turbulence, Warwick 1980*, edited by D. A. Rand and L.-S. Young (Springer, New York, 1981), Vol. 898, p. 99.
- ³¹E. Knobloch and D. R. Moore, "Minimal model of binary fluid convection," *Phys. Rev. A* **42**, 4693 (1990).
- ³²V. I. Yakushin, "The instability of fluid motion of a liquid in a thin spherical layer," *Fluid Dyn.* **4**, 83 (1969) [Transl Izv. AN SSSR, Mekh. Zhidosti Gaza **4**, 119 (1969)].
- ³³E. Knobloch, "Bifurcations in rotating systems," in *Theory of Solar and Planetary Dynamos: Introductory Lectures*, edited by M. R. E. Proctor and A. D. Gilbert (Cambridge University Press, Cambridge, 1992).